Supporting Information: Coherent light emission and electrical tuning of WS_2-WSe_2 interlayer excitons

Shengyu Shan,[1,*] Antti J. Moilanen,[1,2,†] Jonas D. Ziegler,[1] Qia Lin,[1] Guodong Xue,[3] Karolina Łempicka-Mirek,[1] David R. Callegari,[4] Takashi Taniguchi,[5] Kenji Watanabe,[6] Kirsten Moselund,[4] Kaihui Liu,[3] Simone Iadanza,[4] and Lukas Novotny[1,‡]

[1] *Photonics Laboratory, ETH Zürich, 8093 Zürich, Switzerland*
[2] *Center for Photonics Sciences, University of Eastern Finland, FI-80100 Joensuu, Finland*
[3] *State Key Laboratory for Mesoscopic Physics, Frontiers Science Center for Nano-optoelectronics, School of Physics, Peking University, Beijing 100871, China*
[4] *Paul Scherrer Institute, 5232 Villigen, Switzerland*
[5] *Research Center for Materials Nanoarchitectonics, National Institute for Materials Science, 1-1 Namiki, Tsukuba 305-0044, Japan*
[6] *Research Center for Electronic and Optical Materials, National Institute for Materials Science, 1-1 Namiki, Tsukuba 305-0044, Japan*

(Dated: May 18, 2026)

CONTENTS

* These two authors contributed equally
† These two authors contributed equally; antti.moilanen@uef.fi
‡ lnovotny@ethz.ch

Supplementary Note 1. Photonic crystal cavity fabrication protocol

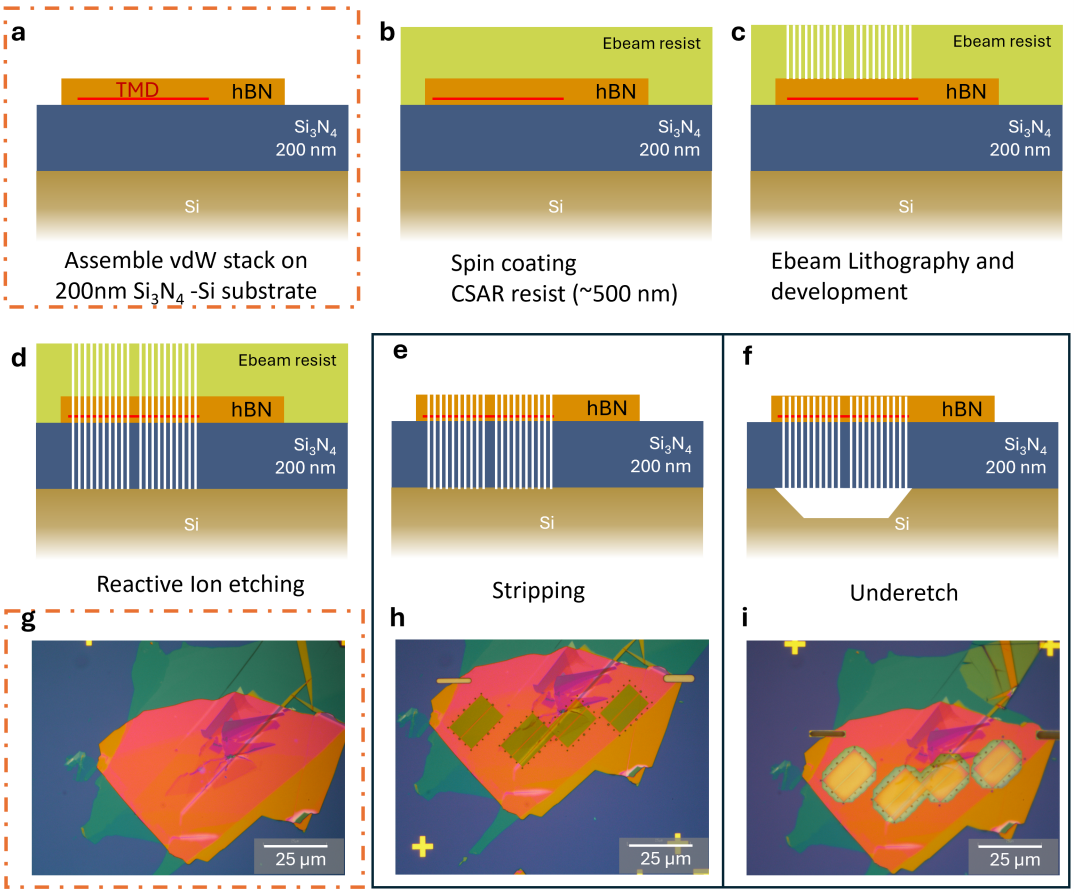

FIG. S1. Fabrication flow of the cavity patterning. **a**, Sketch of the sample after stacking. **b** spin coating Ebeam resist (CSAR 6200.13). textbfc, Electron beam (Ebeam) lithography and development. **d**, Dry etching of hBN and Si_3N_4. **e**, stripping of Ebeam resist. **f** suspension of the cavity via Si underetching. **g**, **h** and **i** are the optical image of Sample A corresponding to the step in **a**, **e**, and **f**

Figure S1 illustrates the fabrication workflow for the photonic crystal cavity patterning process. Initially, the vdW stack is transferred onto the substrate as shown in Fig. S1**a**. The stack surface was treated with O_2 plasma at 100 W and 1 mbar for 30 s to enhance adhesion between the hBN and the electron beam resist. Subsequently, CSAR 6200.13 resist was spin-coated at 2600 rpm to a thickness of approximately 500 nm. The resist was baked at 85 °C for 1 min followed by 150 °C for 2 min. This O_2 plasma treatment is critical to prevent the resist from cracking at the corners during the development stage. Electron beam (Ebeam) lithography was executed using an EBPG 5200 system with a 100 kV acceleration voltage. Following exposure, the sample was developed in amyl acetate at room temperature for 1 min, immersed in isopropanol for 1 min for stopping, and gently dried using a N_2 gun (Fig. S1**c**). Finally, the sample was post-baked at 130 °C for 2 min to improve its dry etching resistance.

Figure S1**d** shows the device structure after dry etching process. For sample A and C, etching was performed using an inductively coupled plasma reactive ion etching (ICP-RIE) system (ICP 100 OXFORD) and followed by a RIE system (Oxford PlasmaLab system 80 RIE). In ICP-RIE stage, an Ar flow of 20 sccm and SF_6 of 5 sccm were used with an ICP power of 300 W and an RF power of 50 W. The etching and strike pressure were set to 2 mbar and 5 mbar, respectively. The sample was etched continuously for 120 s to etch through the vdW stack, which mainly hBN with thickness ~100 nm). Then RIE was used to etch through the remaining Si_3N_4. The recipe was set to have O_2 5 sccm, CHF_3 50 sccm, pressure 55 mbar and RF power of 150 W. The sample was etched for 150 s to 210 s to etch through Si_3N_4. Sample B and D was processed using only the RIE for both vdW stack (hBN) and Si_3N_4 etching. For hBN etching, the parameters were 20 sccm Ar and 2 sccm SF_6 at 95 W RF power, with etching and strike pressures of 10 mbar and 35 mbar.

Figure S1**e** shows the resist stripping process. O_2 descum ($\sim$75 W, 150 s, 1 mbar) was used to remove the cross-linked resist. The remaining resist was stripped in AR 600-71 (4 min, room temperature), then rinsed in acetone and isopropanol. Finally, the sample was immersed in a 40% KOH aqueous solution overnight at room temperature for underetching. Figures. S1**g**, **h**, and **i** show the optical microscope image of sample A after stacking, stripping, and underetching, respectively. Additional holes surrounding the cavity are used to facilitate the underetching process and enhance the out-scattering of the cavity mode. Observation windows located at the edge of the stack (Fig. S1h, i) served to monitor the etching depth in step d. However, additional etching time is required to compensate for RIE lag, where smaller features such as photonic crystal cavity holes etch slower than the larger observation windows. If the Si_3N_4 was not etched through before resist removal, underetching will not occur. It is possible to further etch the sample in RIE without the resist, but the Q factor can be lower ($\lesssim 2000$) due to the increased surface roughness.

Supplementary Note 2. Cavity optimization via lithographical tuning

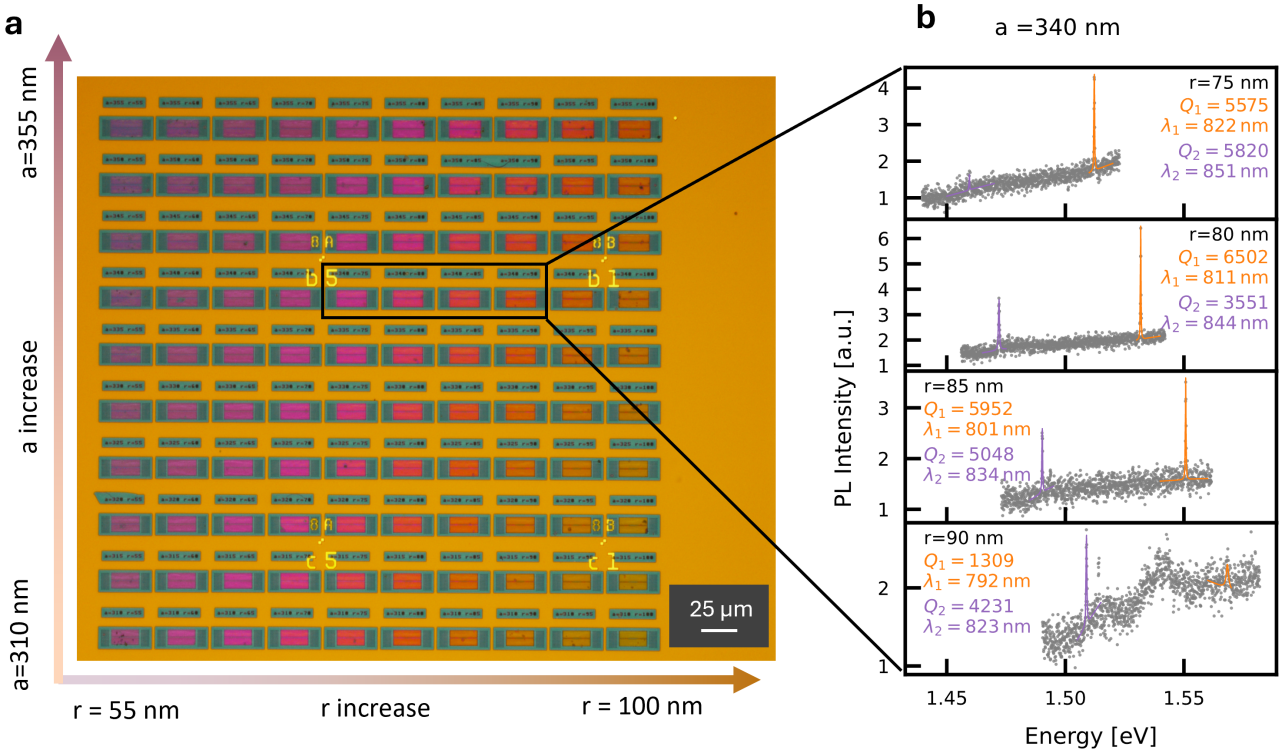

FIG. S2. **a**, Array of photonic crystal cavities with systematically varied lattice constant (a) and hole radius (r) for lithographical tuning. **b**, Measured cavity resonances for devices with $a = 340$ nm and varying r. Two modes with high Q are fitted by Lorentzian functions (orange: mode 1, purple: mode 2). Increasing the hole radius reduces the effective refractive index, leading to a blue shift of the cavity resonance.

Simulations initially assumed a refractive index of $n = 2.05$ for both hBN and Si_3N_4. In practice, process-induced variations—such as refractive index deviations and systematic lithographic offsets—shift the cavity resonance. Lithographical tuning was therefore performed to calibrate these effects and validate the robustness of the cavity design. This process confirms that high-Q modes are reproducible experimental features rather than numerical artifacts. It further identifies the accessible parameter space for the lattice constant (a) and hole radius (r) relative to fabrication biases.

For initial design verification, a substrate with 300 nm low-pressure chemical vapor deposition (LPCVD) Si_3N_4 (WNA40525255B1314S301, MicroChemicals GmbH) was used for lithographical tuning instead of the hBN (∼100 nm)–Si_3N_4 (∼200 nm) heterostructure. Omitting the hBN layer removed the constraint imposed by the limited flake size and enabled fabrication of a large array of photonic crystal cavities with systematically varied lattice constants (a) and hole radii (r), as illustrated in Fig. S2**a**.

To characterize the cavity resonances in Si_3N_4, we utilized its intrinsic background PL of Si_3N_4 at room temperature using setup 2. This background PL is broad and centered near 850 nm, and can be detected under CW excitation at 633 nm with a power of ∼1 mW. The background emission is strongly quenched at cryogenic temperatures (∼4 K), ensuring negligible influence on the interlayer exciton measurements.

Figure S2**b** shows cavity spectra for devices with a lattice constant of $a = 340$ nm and different hole radii (r). Two resonant modes with high Q factors are fitted using Lorentzian profiles (orange: mode 1, purple: mode 2). Mode 1 exhibits a fitted Q exceeding 6000, limited by the spectrometer resolution, confirming that the design supports high-Q resonances. Increasing the hole radius (r) leads to a systematic blue shift of the cavity modes, consistent with the simulations. It also indicates that the design is robust, as high-Q resonances persist over a range of geometrical parameters.

Aligning the cavity resonance with the interlayer exciton wavelength requires accounting for three primary factors:

(i) the actual hole size after fabrication, (ii) the refractive index of the Si_3N_4 layer, and (iii) the thickness of the hBN encapsulation. SEM analysis shows that the fabricated hole radii on the Si_3N_4 surfaces are typically ∼22 nm larger than the design values, whereas in the hBN (∼100 nm)–Si_3N_4 (∼200 nm) heterostructure, the fabricated holes are about ∼5 nm larger than designed. This can be related to different Ebeam resist thickness and etching dynamics between Si_3N_4 and hBN. Ellipsometry measurements further reveal that the 300 nm Si_3N_4 film has a refractive index of approximately 2.0 near 850 nm (Fig. S3**a**), while the thinner 200 nm layer used in the vdW-integrated devices exhibits a higher index of $n \approx 2.18$ (Fig. S3**b**). Although the optical properties of Si_3N_4 are not expected to depend directly on film thickness, variations in the deposition conditions between wafers can alter the Si:N ratio and consequently change the refractive index [1]. Both the reduced hole size and the increased refractive index predict a significant red shift for resonances in the hybrid cavities. To calibrate these factors alongside the influence of hBN thickness, hybrid hBN–Si_3N_4 cavities, with and without integrated CVD TMDs, were fabricated at multiple iterations.

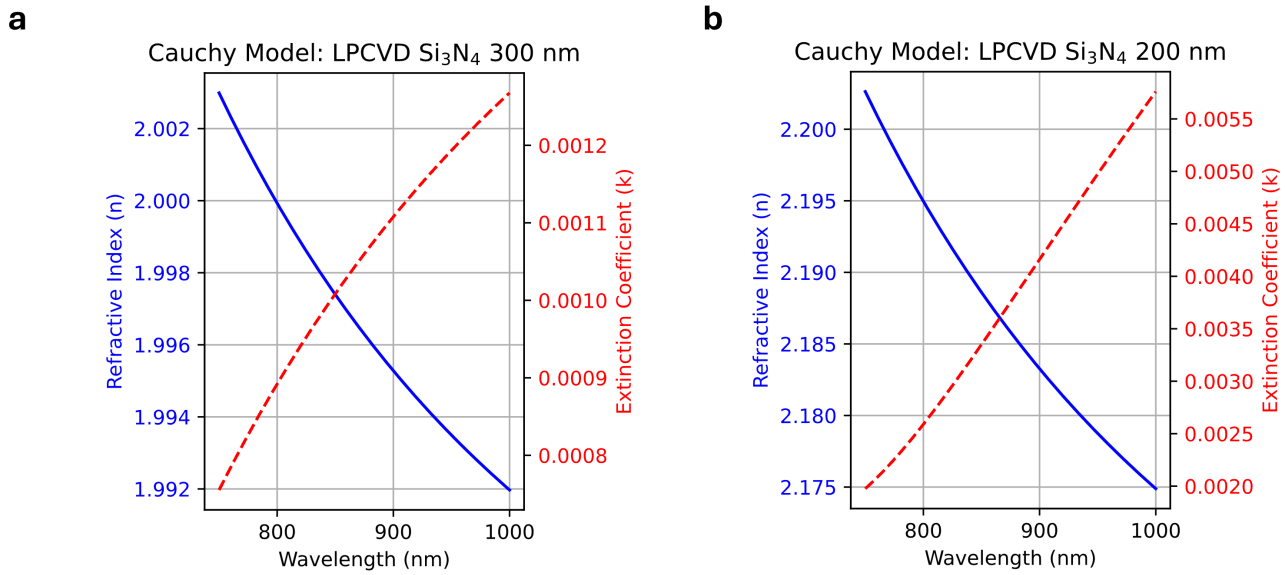

FIG. S3. **a**, Refractive index of the 300 nm Si_3N_4 film used for lithographical tuning, measured by ellipsometry and fitted using a Cauchy model. **b**, Refractive index of the 200 nm Si_3N_4 film used in the vdW-integrated samples (Samples A and C), measured and fitted using the same model.

Considering both the fabrication bias and the refractive-index variation, we selected $a = 340$ nm and $r = 85$ nm as the optimal design for the vdW-integrated samples (Samples A and B), providing the desired resonance wavelength while maintaining high Q. To compensate for variations in hBN thickness and interlayer exciton energy among different samples, an in-plane scaling factor of 95–105% can be applied to the design parameters.

Supplementary Note 3. Cavity resonance measurement from scatterer

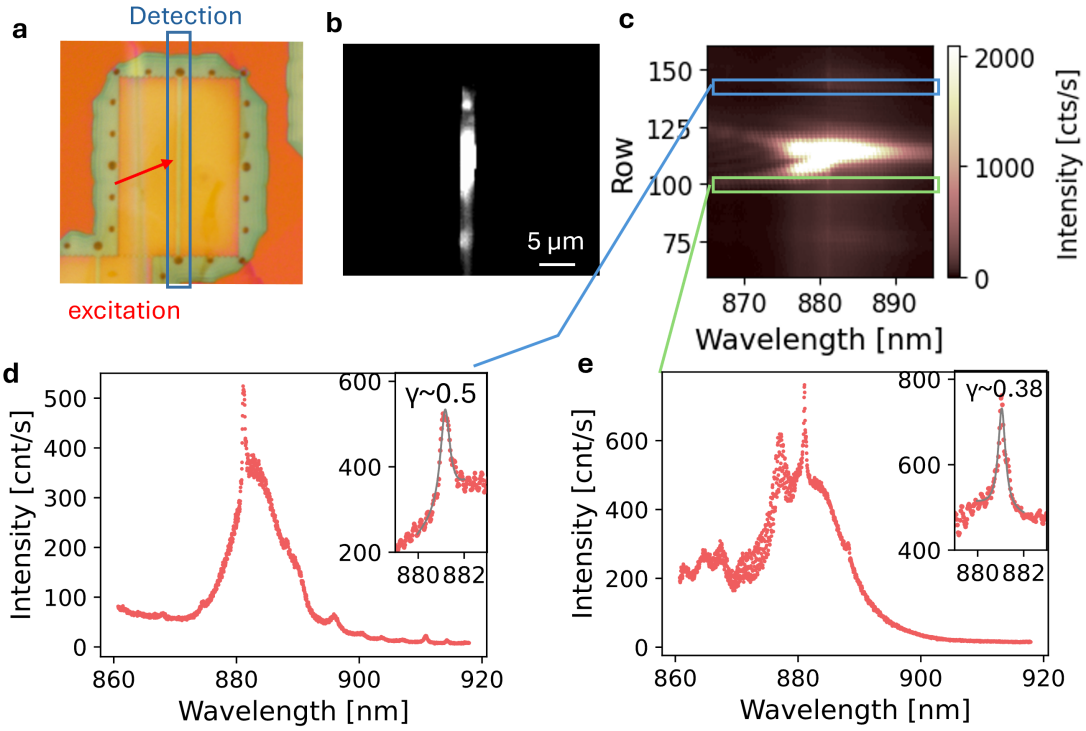

FIG. S4. **a**, Optical image of sample A after cavity fabrication. **b**, Spectrometer image taken at the 0th order. **c**, 2D PL spectrum measured under 633 nm excitation with an incident power of 22 μW on sample. **d**, Spectrum integrated over rows 142–144, and **e**, over rows 99–101. Insets show Lorentzian fits to the cavity modes, with the extracted full width at half maximum (FWHM) γ indicated. The fitting equation is a linear background plus Lorentzian: $y = A\frac{\gamma^2/4}{(\lambda-\lambda_0)^2+\lambda^2/4} + k\lambda + b$, where A is the amplitude, λ_0 is the resonance wavelength, and k and b describe the linear background.

Figure S4 shows the method of measuring cavity resonance from the scatterer. Figure S4**a** displays the optical microscope image corresponding to sample A after patterning. The red arrow indicates that the incident laser is focused at the cavity center. A hole (diameter ~600 nm) at the end of the defect line serves as a scatterer for the cavity mode. The defect line was aligned to be parallel to the spectrometer entrance slit. Figure S4**b** shows shows the PL image of the defect line captured at the 0th order of the grating. The central emission region contains a combination of cavity-uncoupled and other mode-coupled light emission PL. Conversely, two scatterers are clearly visible at the top and bottom of the slit image, and are less effected by other modes. Figure S4**c** presents a representative 2D spectrum of this configuration.

By integrating selected rows, the cavity resonances can be extracted either from the scatterers or from regions near the cavity center. Spectra obtained from the scatterer (Fig. S4**d**) generally show cleaner cavity-resonance features. This may indicate that light from low-Q modes or uncoupled interlayer excitons preferentially scatters directly from their generation sites, whereas high-Q modes experience lower radiation loss and remain more confined within the cavity. Near the cavity center, the spectral resolution is higher. Therefore, in the following analysis, the resonance fitting was performed using spectra from the central rows (rows 99–101), while the Michelson-interferometry–based coherence measurements were carried out using emission from the scatterer for a higher signal-to-noise ratio.

Supplementary Note 4. Rate–equation model for L–L curve fitting

Laser rate equations

The laser dynamics are described by the standard semiconductor laser rate equations [2]:

$$\frac{dN}{dt} = R_{\text{in}} - \frac{N}{\tau} - v_g\, g(N)\, S, \tag{S1}$$

$$\frac{dS}{dt} = \Gamma\, v_g\, g(N)\, S + \beta\, \frac{N}{\tau} - \frac{S}{\tau_p}, \tag{S2}$$

where N is the carrier number, S is the photon number, R_{in} is the pump rate, τ is the carrier lifetime, τ_p is the photon lifetime, v_g is the group velocity, Γ is the optical confinement factor of the cavity, and β is the spontaneous emission coupling factor.

Linear gain model

The material gain is assumed to be linear in carrier density:

$$g(N) = a\,(N - N_{\text{tr}}), \tag{S3}$$

where a is the differential gain and N_{tr} is the transparency carrier number.

Parameter definitions

For compactness, the following parameters are introduced:

$$a' = a\, v_g\, \tau, \tag{S4}$$

$$c = \Gamma\, \tau_p\, \frac{\eta}{V} \tag{S5}$$

where η is the pump absorption efficiency and V is the cavity mode volume.

Closed–form steady–state solution

Setting $dN/dt = dS/dt = 0$ yields a quadratic equation for the steady–state photon number. The physically relevant solution is:

$$S(N_{\text{in}}) = \frac{A}{2a'} \left[a' c N_{\text{in}} - 1 + \sqrt{(a' c N_{\text{in}} - 1)^2 + 4a'\beta c N_{\text{in}}} \right]. \tag{S6}$$

This expression is used to fit the measured L–L curve and extract the spontaneous emission coupling factor β. The parameters used in the least-squares fitting are given in Table S1; spontaneous emission coupling factor β and a scaling constant A as fit parameters.

TABLE S1. Parameters used in the rate–equation model for L–L curve fitting.

Symbol	**Value & Unit**	**Description**
τ	50 ns	Exciton lifetime
τ_p	$Q\lambda_0/(2\pi c) = 1.25$ ps	Photon lifetime (c = speed of light)
Q	2681	Cavity Q-factor
λ_0	881 nm	Cavity photon wavelength
v_g	$1E+7$ cm/s	Exciton group velocity in the active medium
Γ	0.01	Optical confinement factor of the cavity
a	1E-16 cm^2	Differential gain coefficient
V	2.83E-13 cm^3	Cavity mode volume
η	0.20	Pump absorption efficiency

Supplementary Note 5. Michelson interferometry with spectrometer for coherence time measurement

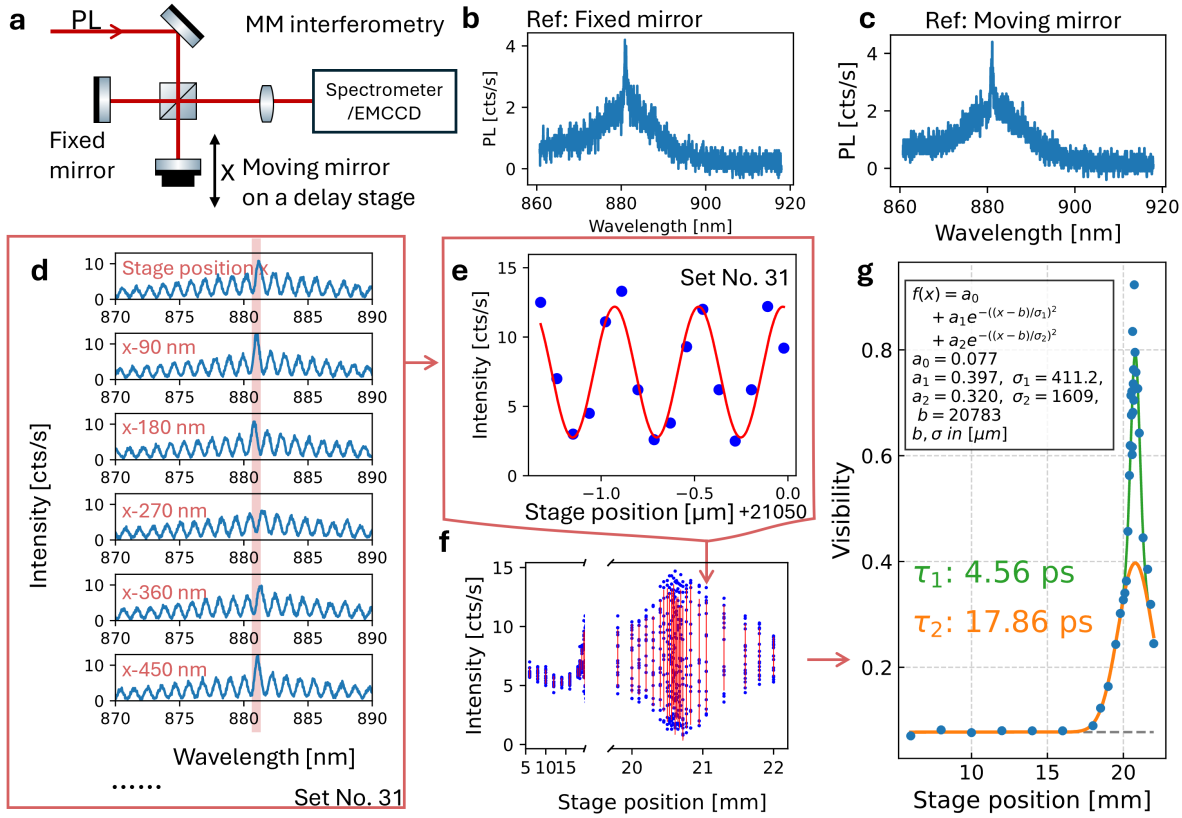

FIG. S5. **Michelson interferometry for coherence time measurement.** **a**, Schematic of the Michelson interferometer setup used to measure the first-order field correlation function $g^{(1)}(\tau)$. **b**,**c** Reference spectra recorded from each arm individually, showing nearly identical cavity modes at $\lambda \approx 881$ nm. **d**, Six representative interference spectra from one delay set. The first spectrum corresponds to a delay of $x = 21\,050$ µm, which is about 270 µm offset from zero delay. Each subsequent spectrum is acquired after moving the delay stage by ~ 90 nm. The pink bar indicates the cavity mode position. One delay set contains 16 spectra in this example. **e**, Intensity oscillations of a single spectrometer pixel corresponding to the cavity mode wavelength in one delay set, fitted with a sinusoidal function with a constant offset. Blue dots are measured data points, and the red curve is a fit. **f**, Intensity oscillations of this pixel extracted from multiple delay sets, showing the decay of the interference contrast. **g**, Fringe visibility obtained after normalization and averaging over a few neighboring pixels, fitted with Gaussian functions to extract the coherence time.

The Michelson interferometer setup is illustrated in Fig. S5(a). Collimated PL from the sample is directed to a 50:50 beamsplitter, which splits the light into two arms. One mirror is fixed, while the other is mounted on a motorized delay stage. After reflection, the two beams recombine and interfere at the beamsplitter, and the output is sent to a detector, either an EMCCD camera or a spectrometer, depending on the cavity linewidth. By scanning the delay stage and recording interference patterns, we extract $V(\tau)$ and thus the coherence time.

Data acquisition and analysis

Figures S5**b**–**g** illustrate the data acquisition and analysis workflow. Figures S5**b**, and **c** display two reference spectra recorded from the individual interferometer arms. These spectra are nearly identical and feature a cavity mode near 881 nm. The linewidth of this mode is below 0.5 nm. With both arms unblocked, we record sets of interference spectra while stepping the delay stage by ~ 90 nm between successive acquisitions. In this example, each set consists of 16 spectra, with six representative examples shown in Fig. S5**d**. The oscillatory intensity modulation at a single spectrometer pixel corresponding to the cavity mode wavelength is fitted with a sinusoidal function with an offset (Fig. S5**e**). By repeating this procedure over multiple delay sets, we track the amplitude decay as a function of delay

(Fig. S5**f**). Finally, after normalizing and optionally averaging over neighboring pixels, we obtain the visibility ($V(\tau)$) at different delay stage positions as shown in Figure S5**g**. The results are fitted with one or more Gaussian functions to extract the corresponding coherence time, as shown in Fig. S5**g**. For a Gaussian distribution $f(x) = a_0 e^{-(\frac{x-b}{\sigma})^2}$, the FWHM is $2\sqrt{\ln 2}\,\sigma$, and the coherence time is:

$$\tau = 2 \cdot \frac{2\sqrt{\ln 2}\,\sigma[\mu\text{m}]}{c\ [\mu\text{m/ps}]} \approx 0.11\sigma[\text{ps}], \tag{S7}$$

in which the factor 2 comes from the additional delay in the round-trip of light mirror, σ in the unit of μm and the light speed c is 300 µm/ps.

In the following, we provide a more detailed derivation for the relation between the incident field (under filtering) and the resulting coherence measurement. We prove that as long as the incident spectra is narrower than the filter, i.e. spectral resolution limit of the spectrometer, we can recover the coherence time of the resonance feature.

Field representation and spectral description

To relate temporal coherence to spectral properties, we assume that (1) the paraxial condition is fulfilled, (2) the apparatus is insensitive to polarization, and (3) we consider field points $\mathbf{r}$ within the transverse coherence length from the optical axis. In this case, we can approximate $E(\mathbf{r}, t)$ as a scalar field $E(t)$.

The incident field can be represented by its Fourier transform $\hat{E}(\omega)$ as

$$E(t) = \int_{-\infty}^{\infty} \hat{E}(\omega) e^{-i\omega t}\, d\omega \tag{S8}$$

The autocorrelation function of the field, also called the coherence function, is $\langle E^*(t)E(t+\tau)\rangle_t$, where $\langle\cdot\rangle_t$ indicates the time average with respect to t. The power spectral density $S(\omega)$ of the field is the Fourier transform of the correlation function, that is

$$S(\omega) = \frac{1}{2\pi} \int_{-\infty}^{\infty} \langle E^*(t)E(t+\Delta t)\rangle_t e^{i\omega\tau}\, d\tau \tag{S9}$$

from which we obtain the intensity

$$I_0 = \varepsilon_0 c\, \langle E^*(t)E(t)\rangle_t = \varepsilon_0 c \int_{-\infty}^{\infty} S(\omega)\, d\omega \tag{S10}$$

First-order coherence and fringe visibility

The first-order correlation function (complex degree of coherence) for the electric field is defined as:

$$g^{(1)}(\Delta t) = \frac{\langle E^*(t)E(t+\Delta t)\rangle_t}{\langle |E(t)|^2\rangle_t}, \tag{S11}$$

where $E(t)$ is the complex electric field of the emission and $\langle\cdot\rangle_t$ denotes a time average. In a Michelson interferometer, The time delay Δt and stage delay Δx are linked with speed of light c, i.e. $\Delta t = 2\Delta x/c$. The detected intensity with delay Δt is :

$$I(\Delta t) = I_{\text{mov}} + I_{\text{fix}} + 2\sqrt{I_{\text{mov}} I_{\text{fix}}}\, \text{Re}[g^{(1)}(\Delta t)], \tag{S12}$$

where I_{mov} and I_{fix} denote the intensities reflected from the moving and fixed mirrors, respectively. When the phase of $g^{(1)}$ is 0 or π, we reach maximum and minimum intensity:

$$I_{\max} = I_{\text{mov}} + I_{\text{fix}} + 2\sqrt{I_{\text{mov}} I_{\text{fix}}}|g^{(1)}(\Delta t)| \tag{S13}$$

$$I_{\min} = I_{\text{mov}} + I_{\text{fix}} - 2\sqrt{I_{\text{mov}} I_{\text{fix}}}|g^{(1)}(\Delta t)| \tag{S14}$$

where $I_{\max}$ and $I_{\min}$ are the maximum and minimum detected intensities near a given time delay Δt.

Then we have the relation between the fringe visibility $V(\Delta t)$ and related to $g^{(1)}(\Delta t)$:

$$V(\Delta t) = \frac{I_{\max} - I_{\min}}{I_{\max} + I_{\min}} \tag{S15}$$

$$= \frac{2\sqrt{I_{\mathrm{mov}} I_{\mathrm{fix}}}}{I_{\mathrm{mov}} + I_{\mathrm{fix}}} |g^{(1)}(\Delta t)|, \tag{S16}$$

In the case of a 50:50 beam splitter, where $I_{\mathrm{mov}} = I_{\mathrm{fix}}$, this simplifies to $V(\Delta t) = |g^{(1)}(\Delta t)|$. The coherence time τ_{coh} is typically defined as the full width at half maximum (FWHM) of $|g^{(1)}(\Delta t)|$, and can be obtained from the fringe visibility measurements.

Relation between spectrum linewidth and coherence

For input signal with power spectral density $S(\omega)$, the Michelson interferometer renders

$$\begin{aligned} I(\Delta t) &= \frac{1}{4}\varepsilon_0 c \big\langle (E^*(t) + E^*(t+\Delta t))(E(t) + E(t+\Delta t)) \big\rangle_t \\ &= \frac{1}{2}\varepsilon_0 c \int_{-\infty}^{\infty} S(\omega)[1 + \cos(\omega \Delta t)]\, d\omega \end{aligned} \tag{S17}$$

Its output depends on the spectrum $S(\omega)$ of the field. As an example, consider a band-limited field with center frequency ω_0 and bandwidth $\Delta\omega$, which yields

$$I(\Delta t) = S_0 \Delta\omega\, \varepsilon_0 c[1 + \cos(\omega_0 \Delta t)\, \mathrm{sinc}(\Delta\omega \Delta t/2)] \tag{S18}$$

The cosine term is an oscillating function of Δt whereas the sinc function is a localized function defined by the bandwidth $\Delta\omega$. We define the coherence time as the FWHM of the sinc function, that is

$$\tau_{\mathrm{coh}} \approx 1.21 \frac{2\pi}{\Delta\omega} \tag{S19}$$

In other words, the coherence time is entirely determined by the spectral width of the field's power spectral density $S(\omega)$. The narrower the linewidth $\Delta\omega$, the longer the coherence time τ_{coh}.

Effect of spectral filtering

To measure the coherence time of the cavity mode, it is essential to filter out background PL. For broad cavity modes ($\gamma \gtrsim 1\,\mathrm{nm}$), we use a pair of tunable long- and short-pass filters to select the desired wavelength range, followed by intensity detection using an EMCCD camera. However, for narrow cavity modes ($\gamma \lesssim 0.5\,\mathrm{nm}$), filtering with long- and short-pass filters alone leads to significant signal loss and practical challenges. In this regime, we use a spectrometer for detection, which functions as a spectral filter with a resolution comparable to the cavity linewidth.

For a pixel in spectrometer as the detector, we obtain the spectral decomposition of the intensity (S17). This corresponds simply to the integrand:

$$\hat{I}(\Delta t, \omega) = \frac{1}{2}\varepsilon_0 c\, S(\omega)[1 + \cos(\omega \Delta t)] \tag{S20}$$

We integrate the output of the spectrometer around the center frequency ω_0 of the input spectrum $S(\omega)$ with a bandwidth $\Delta\omega$ (the resolving power of the spectrometer):

$$I(\omega_0 \pm \Delta\omega/2, \Delta t) = \frac{1}{2}\varepsilon_0 c \int_{\omega_0 - \Delta\omega/2}^{\omega_0 + \Delta\omega/2} S(\omega)[1 + \cos(\omega \Delta t)]\, d\omega \tag{S21}$$

The result depends on the input spectrum $S(\omega)$, in particular on its bandwidth $\Delta\omega_0$. Assuming the spectrum has Gaussian profile and the bandwidth $\Delta\omega_0$ refers to its FWHM. We consider two limiting cases:

(1) $\Delta\omega_0 \gg \Delta\omega$. The input spectrum is much wider than the integration range $\Delta\omega$ and we can assume $S(\omega) \approx S_0$. Integrating over the range $\omega_0 \pm \Delta\omega/2$ yields the same result as Eq. (S18), with the difference that $\Delta\omega$ now corresponds

to the resolving power of the spectrometer and not to the spectral width of the incident field $E(t)$. In other words, the better the spectrometer, the larger the coherence time.

(2) $\Delta\omega_0 \ll \Delta\omega$. The input spectrum is much narrower than the integration range $\Delta\omega$. To evaluate Eq. (S21), we assume a Gaussian input spectrum centered at ω_0,

$$S(\omega) = S_0 e^{-\frac{(\omega-\omega_0)^2}{\sigma_\omega^2}}, \tag{S22}$$

whose FWHM is

$$\Delta\omega_{\mathrm{FWHM}} = 2\sqrt{\ln 2}\,\sigma_\omega. \tag{S23}$$

In wavelength units, we have approximately

$$\Delta\lambda_{\mathrm{FWHM}} \approx \frac{\lambda_0^2}{2\pi c}\,\Delta\omega_{\mathrm{FWHM}} = \frac{\lambda_0^2}{2\pi c}\,2\sqrt{\ln 2}\,\sigma_\omega. \tag{S24}$$

Evaluating Eq. (S21) in the limit $\Delta\omega_0 \ll \Delta\omega$ yields

$$I(\omega_0 \pm \omega/2, \Delta t) = \sqrt{\pi}\,\varepsilon_0 c \frac{\sigma_\omega S_0}{2}\left[1 + e^{-\sigma_\omega^2 \Delta t^2/4}\cos(\omega_0 \Delta t)\right]. \tag{S25}$$

The interferogram consists of oscillations with period $2\pi/\omega_0$, modulated by a Gaussian envelope. The corresponding fringe visibility is

$$V(\Delta t) = e^{-\sigma_\omega^2 \Delta t^2/4}. \tag{S26}$$

Accordingly, the wavelength-domain linewidth and coherence time are related by

$$\tau_{\mathrm{coh}} = \frac{4\sqrt{\ln 2}}{\sigma_\omega}. \tag{S27}$$

The relationship between the input spectral FWHM and the coherence time is, therefore,

$$\tau_{\mathrm{coh}} \cdot \Delta\lambda_{\mathrm{FWHM}} = 8\ln 2\,\frac{\lambda_0^2}{2\pi c}. \tag{S28}$$

In practice, the input signal typically consists of a narrow resonance superimposed on a broad background. Assuming that the power spectral density of the input signal consists of a narrow Gaussian peak centered at ω_0 on top of a broad background S_B, we write:

$$S(\omega) = S_B + S_0 e^{-\frac{(\omega-\omega_0)^2}{\sigma_\omega^2}}, \tag{S29}$$

the fringe visibility can be expressed as:

$$V(\Delta t, \omega) \propto S_B\,\Delta\omega\,\varepsilon_0 c\,\mathrm{sinc}\left(\frac{\Delta\omega \Delta t}{2}\right) + \sqrt{\pi}\,\varepsilon_0 c \frac{\sigma_\omega S_0}{2} e^{-\sigma_\omega^2 \Delta t^2/4}. \tag{S30}$$

Consequently, the broad background emission, when filtered by the spectrometer, exhibits a coherence time limited by the spectral resolution. Any spectral feature significantly narrower than this resolution appears as a second component in the visibility decay, characterized by a much longer coherence time.

Because the spectrometer transmission typically has a tapered (non-rectangular) profile, the measured visibility decay is smoother and shows fewer oscillations than the sinc behavior predicted by Eq. S30. In practice, we approximate the background contribution using a Gaussian profile.

The estimation of the spectral resolution and numerical modeling of the tapered filtering function (based on sample D) are further presented in Figs. S12 and S13.

Supplementary Note 6. Additional data from sample A

Linewidth fitting and limitation from the setup

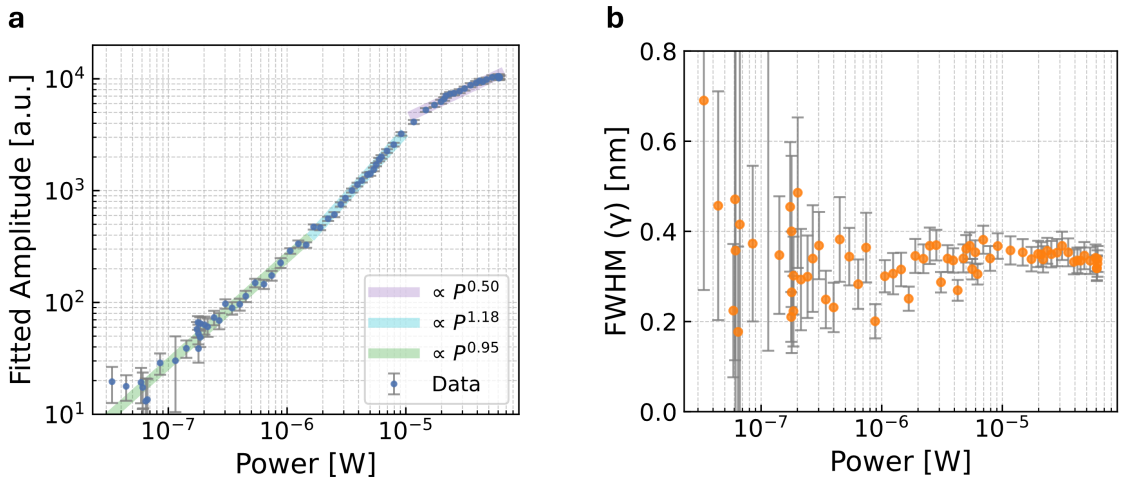

FIG. S6. **a**, Power-dependent amplitude, and **b**, linewidth of cavity mode near 881 nm, row 99-101 (Fig. S4**e**). In **a**, blue dots with grey error bars show the fitted amplitude A and the fitting uncertainty; green, blue, and purple lines represent linear fits with different slopes. The fitting equation for cavity mode is a linear background plus Lorentzian: $y = A\frac{\gamma^2/4}{(\lambda-\lambda_0)^2+\lambda^2/4} + k\lambda + b$, where A is the amplitude, γ is the FWHM, λ_0 is the resonance wavelength, and k and b describe the linear background.

The light-in–light-out (L–L) curve is shown in Fig. S6**a**. It exhibits a slope exceeding ∼1 on a log-log scale over the 1.6 µW–12 µW range, indicating a superlinear increase of output emission. Assuming a diffraction-limited excitation area—defined by the 633 nm pump wavelength and an objective numerical aperture (NA) of 0.81—we estimate that an input power of 1.6 µW corresponds to a power density of $2.24 \times 10^2\,\mathrm{W\,cm^{-2}}$. The fitted linewidths are shown in Fig. S6**b**, typically ranging between 0.2 nm and 0.4 nm. The large number of data points reveals a general linewidth narrowing trend, most pronounced between 100 nW and 1000 nW. This behavior hints an increase in temporal coherence already below 1 µW, however not statistical significant.

Expect for the resolution limit of spectrometer itself, we assume there are mainly two other challenges of measuring linewidth accurately. 1) An additional modulation with a period of approximately 0.3 nm is present in all measured spectra (as can been seen in Fig. S6**b**), which makes the direct linewidth fitting very difficult. The source of the modulation was not found yet, it might be related to the optical window of cooling chamber. 2) The cavity mode were measured from scattered light, but not from directly from where it was generated. As shown in the inset of Fig. S4**d**, the cavity mode was fitted to have a linewidth of 0.5 nm at the scatterer. As rows which corresponding to a position closer to the cavity center (row 99-101, Fig. S6**b**), a cavity linewidth was fitted to be 0.34 nm, which is already narrower. But we cannot directly measure the clear cavity mode from the center of the cavity due to the light emission from uncoupled cavity modes and other cavity modes.

Quantum threshold analysis

Quantum threshold of lasing refers to the fact that at the lasing threshold, the photon number in the cavity state is $\langle n \rangle = 1$ [3]. Here, we can use the cavity Q factor, β factor, and TMD absorption to estimate whether the sample has reached the quantum threshold in the nonlinear regime (1.6 µW to 12 µW).

For pumping power lower than the nonlinear increase, we measured a coherence time of 6.95 for the cavity coupled emission. This corresponds to a linewidth of 0.33 nm at a resonance wavelength of 881 nm, yielding a quality factor $Q = 2681$. At resonance, the photon lifetime τ_{ph} is given by:

$$\tau_{ph} = \frac{Q}{\omega_0} = \frac{Q\lambda_0}{2\pi c} \tag{S31}$$

, where ω_0 is the angular frequency of photon at resonance, and c is the speed of light.

The output power P_{out} of the cavity is related to the energy U stored within the cavity. By expressing energy in terms of the average photon number $\langle n \rangle$, we get:

$$P_{out} = \frac{U}{\tau_{ph}} = \langle n \rangle \frac{hc/\lambda_0}{\tau_{ph}} = \langle n \rangle \frac{2\pi hc^2}{\lambda_0^2 Q} \tag{S32}$$

where h is Planck's constant ($6.626 \times 10^{-34}\,\mathrm{J\,s}$). At the quantum threshold ($\langle n \rangle = 1$), the required output power is:

$$P_{out}^{QT} = \frac{U}{\tau_{ph}} = \frac{h2\pi c^2}{\lambda_0^2 Q} \approx 0.18\,\mu\mathrm{W} \tag{S33}$$

This means the output power for the sample at quantum threshold of lasing should reach 0.18 µW.

Our observed nonlinear regime spans incident powers from 1.6 µW to 12 µW. Pinpointing a single threshold value is challenging due to density-dependent interlayer exciton dynamics, such as blue-shifts and exciton-exciton annihilation. However, we can estimate the effective output power based on the following physical parameters: 1) Absorption: we approximate the heterobilayer TMD absorption at 633 nm is $\sim$ 20%, i.e. each TMD monolayer has absorption on the order of 10% [4]. 2) Conversion: we assume near-unity conversion of intralayer excitons to interlayer excitons, supported by the fact that intralayer exciton PL intensity is typically orders of magnitude weaker than interlayer exciton PL. 3) Coupling (β): based on rate-equation fitting, we estimate that 30% of interlayer excitons couple to the cavity mode. Under these assumptions, an incident power range of 1.6 µW–12 µW translates to an output power of approximately 0.07 µW to0.52 µW. Since this range encompasses the predicted $P_{out}^{QT} = 0.18\,\mu\mathrm{W}$, our results are consistent with the system reaching the quantum threshold of lasing.

In the above calculation, the internal quantum yield (QY) of the interlayer exciton was assumed to be unity. In reality, the quantum threshold is still achieved in the nonlinear increase region if the quantum yield is no less than 40%.

An alternative approach to estimating the output power involves back-calculating from the detected spectra, accounting for the optical setup spectral transmission and collection efficiency. However, while the transmission function of the optical setup is well-characterized, the out-coupling from the cavity mode occurs via a scatterer. The unknown radiation pattern and directional efficiency of this scattering process preclude a precise quantitative estimation of the total out-coupled power. Future implementations utilizing architectures with well-defined out-coupling efficiencies, such as integrated grating couplers or waveguide-coupled collectors, will be helpful in determine when the system is reaching quantum threshold.

Supplementary Note 7. Additional results from sample B

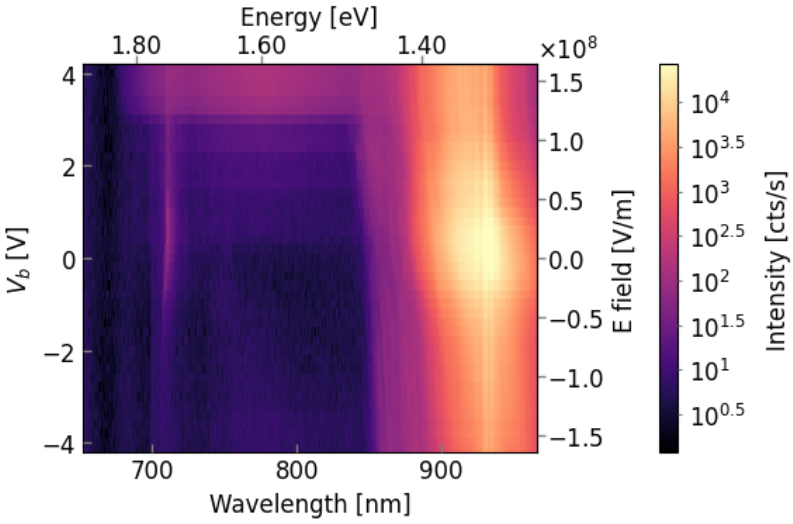

FIG. S7. Bias dependent PL spectra of cavity coupled intra- and interlayer excitons. These data correspond to the same measurement series presented in figure 4**d** of the main text, here plotted on a logarithmic scale without normalization. PL intensity is reported as raw detector counts per second [cts/s] without instrument response corrections. To maximize the signal-to-noise ratio for the intralayer exciton features, each horizontal line in this map represents a binning of spatial rows corresponding to both the cavity center and the scatterer positions. While the bining range of figure 4**d** in the main text only include the scatterer positions to provide a clearer representation of the cavity modes. The observed intensity trends for both intra- and interlayer excitons remain consistent across both binning ranges.

As shown in Fig. S7, interlayer exciton PL intensity decreases with increasing bias for both polarities and exhibits irregular discontinuities in sample B. The change in PL intensity may be associated with injected carriers. Although the WSe_2–WS_2 heterobilayer is not in direct contact with the electrodes, we detect a leakage current of approximately 13 pA at 4 V. This current could influence the electron filling factors, defined as the number of electrons per moiré unit cell. Such fluctuations in filling factors are known to trigger discontinuous changes in the emission spectra of moiré systems [5]. It has also been reported that non-radiative recombination processes can scale with the induced carrier density [6], which could explain the reduced interlayer exciton PL intensity at higher bias.

Supplementary Note 8. Additional results from sample C

lifetime measurement before and after patterning

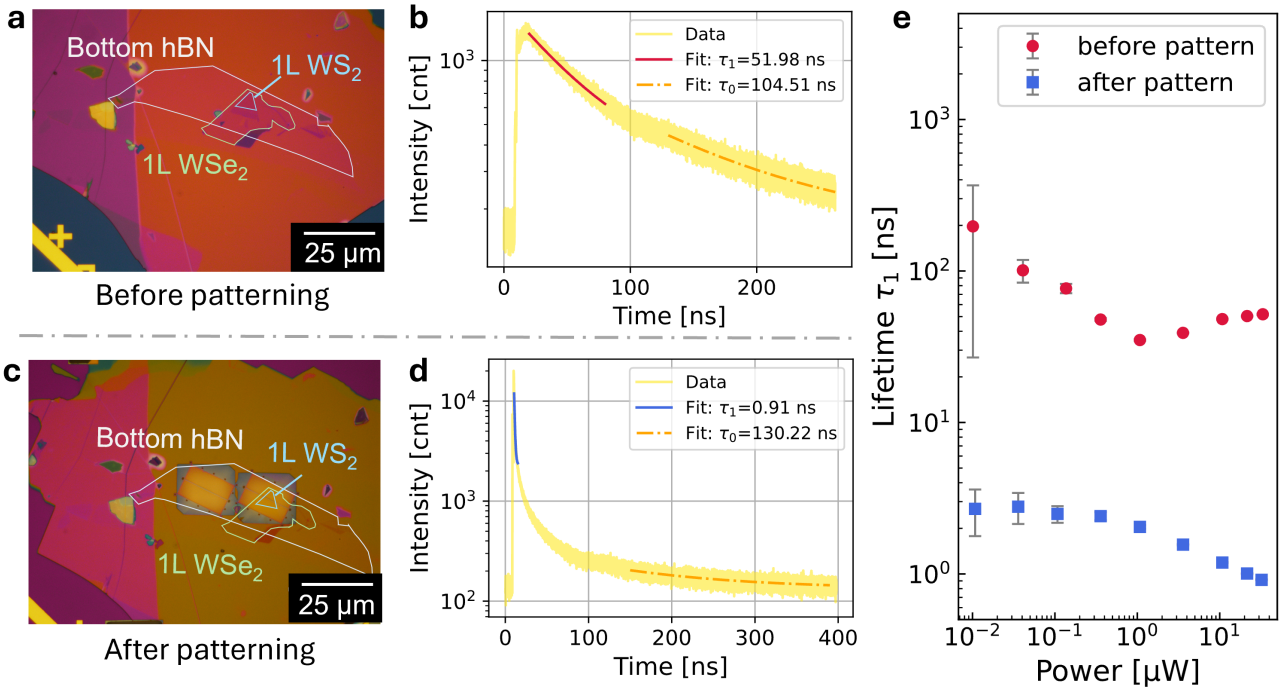

FIG. S8. **a**, Optical image of sample B before, and **c**, after cavity patterning. **b**, Time-resolved PL (TRPL) of interlayer exciton before patterning, and **d**, after patterning, both with average excitation power of 33 µW . Two temporal regions in each decay curves were fitted separately by exponential decay to obtain a faster and a slower decay term. **e** Power-dependent short lifetime (τ_1) of the interlayer exciton before and after patterning.

Sample C is a reference sample, which has a similar structure to sample A. The sample is composed of top hBN(∼90 nm)/1L WSe_2/1L WS_2/bottom hBN (∼5 nm) and the optical image of sample C before and after patterning is shown in Fig. S8**a**. The time-resolved measurements are performed using a pulsed laser diode (Picoquant LDH-D-C-640) with a repetition rate of 2.5 MHz and pulse widths below 90 ps. The signal is filtered using a 700 nm long pass filter and detected by a Single Photon Avalanche Diode (MPD-020-CTF), which is time-correlated with the pulsed laser (Picoharp 300). The total temporal instrument response function exhibits a FWHM of around 0.28 ns. The measured photon counts versus delay give the information of interlayer exciton lifetime.

The intralayer exciton light emission was much weaker than that of the interlayer exciton in sample C, and was therefore assumed to have a negligible contribution to the lifetime measurement. The TRPL trace measured before patterning, using an average excitation power ∼ 33 µW, is shown in Fig. S8 **b**. The decay curve was fitted with a single-exponential function in two distinct temporal regions to extract the characteristic lifetimes. Data near 120 ns was excluded from the fit due to the measurement artifacts. The interlayer exciton exhibited significantly longer lifetimes than typical monolayer excitons [7, 8], with a fast decay component near 50 ns and a slow component exceeding 100 ns.

After patterning photonic crystal cavities, an optical image of the sample is shown in Fig. S8**c**. The sample was overetched by ∼ 10 nm due to the incomplete etching before resist removal, resulting a resonance Q factor ∼2000 for mode 1. The TRPL trace shown in Fig. S8**d** was measured with the excitation laser focused at the cavity center under an average excitation power of ∼ 33 µW. The fastest decay component exhibits a lifetime of 0.91 ns, corresponding to a lifetime shortening factor of ∼ 57.

The extracted short lifetime τ_1 before and after patterning was plotted as a function of excitation power, as shown in Fig. S8**e**. Before patterning, the lifetime decreases with increasing excitation power, which we attribute to the density-dependent interactions and loss channels [7]. After patterning, the lifetime shortening ratio ranges between 17 and 60, and also shows a power-dependent behavior. This behavior is likely related to the power-induced blue shift of the interlayer exciton energy, which modifies its detuning and coupling with multiple nearby cavity modes. The

decrease of lifetime at higher power might be an indication of stimulated emission.

The Purcell factor of a single mode can also be calculated based on the cavity Q factor, and the alignment of cavity mode and emitter [9]:

$$F_P = \frac{3}{4\pi^2}\left(\frac{\lambda_{\text{free}}}{n}\right)^3 \frac{Q}{V_{\text{mode}}} \cdot \xi, \tag{S34}$$

where λ is the resonant wavelength, n is the refractive index of the medium, Q is the cavity Q factor, V_{mode} is the mode volume defined by [10]

$$V_{\text{mode}} = \frac{\int \varepsilon(\mathbf{r})|\mathbf{E}(\mathbf{r})|^2\, dV}{\max\left[\varepsilon(\mathbf{r})|\mathbf{E}(\mathbf{r})|^2\right]}, \tag{S35}$$

where the maximum of the electric field of the cavity fundamental mode is at the geometrical center of the cavity, r=(0,0,0). The mode overlap factor ξ accounts for the spatial and dipole alignment between the emitter and the cavity mode. It is defined as:

$$\xi = \frac{|\mathbf{E}(\mathbf{r}_0)\cdot\hat{\mathbf{d}}|^2}{\max|\mathbf{E}(\mathbf{r})|^2|\hat{\mathbf{d}}|^2}, \tag{S36}$$

where $\mathbf{E}(\mathbf{r}_0)$ is the cavity electric field at the emitter position, $\hat{\mathbf{d}}$ is the unit vector of the emitter's dipole orientation, $\max|\mathbf{E}(\mathbf{r})|^2$ is the maximum field intensity in the cavity mode.

Based on the FDTD simulation [11], the mode volume V_{mode} is calculated to be $0.283\,\mu\text{m}^3$. Assuming perfect dipole orientation alignment between the dipole and the cavity electric field, and that the bottom hBN is less than 10 nm in sample C, i.e., the position of the emitter is 60 nm above the field maximum in the z direction, we obtained $\xi = \frac{|\mathbf{E}(\mathbf{r}_0)|^2}{\max|\mathbf{E}(\mathbf{r})|^2}|_{\text{r}_0=60\ \text{nm}} \simeq 0.78$. From the measurement of sample C, we obtained the fundamental mode has a Q factor ~ 2000, central wavelength $\lambda_{\text{free}}\sim$842 nm and we take hBN refractive index of 2.1. Thus, we obtained a enhancement factor of $F_p \sim 27$ for dipole orientation aligned with the cavity mode 1 and being positioned at 60 nm above the cavity center. This value is on the same order as the experimentally observed lifetime shortening factor.

Exciton density estimation

Based on the PL spectra of sample C before patterning, we estimate the exciton density with 7.2 µW excitation (640 nm CW). We detected a photon count rate of $\sim 4\times10^6$ cnt/s at the spectrometer. By calibrating the setup transmission function using a transmission lamp and a red laser, we estimate that the photon entering the objective has a rate of 3.47×10^{10} cnt/s. Assuming the interlayer exciton emission dipole is in-plane, and the objective has a NA of 0.81, we obtain ~3% collection efficiency from the light emitted by the interlayer exciton by performing FDTD simulation in Lumerical. Assuming the quantum efficiency of 100% of the interlayer exciton at cryogenic temperatures, we obtain a lower bound of exciton generation rate of $G = 3.15\times10^{11}$ Hz. Assuming the area of excitation is resolution limited, i.e. the radius of excitation is $r = 0.61\lambda/\text{NA}$, where $\lambda = 640$ nm, $NA = 0.81$, $r \approx$482 nm and the excitation area $A = \pi r^2 \approx 7.3\times10^{-9}\,\text{cm}^{-2}$. The exciton generation rate per area is:

$$g_{ex} = \frac{G}{A} \approx 4.3\times10^{19}\ \text{cm}^{-2}\text{s}^{-1} \tag{S37}$$

Taking interlayer exciton lifetime of 50 ns based on the fitting shown in Fig.S8**c** and **d**, we obtain an lower limit of exciton density with 7.2 µW excitation power before cavity patterning:

$$n_{ex} = \frac{G\times\tau}{A} \approx 2.16\times10^{12}\ \text{cm}^{-2} \tag{S38}$$

After patterning, assuming the same generation rate but a shorter lifetime $\sim$ 1 ns, we have $n_{ex} \sim 4\times10^{10}\,\text{cm}^{-2}$.

Supplementary Note 9. Additional results from sample D

Sample D structure and spectrum

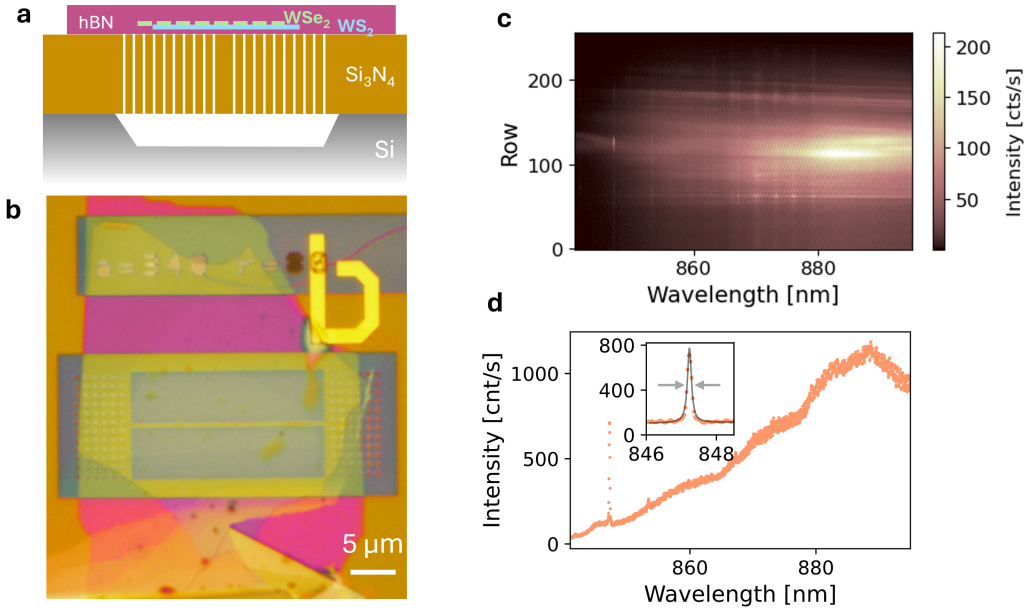

FIG. S9. **a**, Schematic illustration and **b**, optical image of Sample C. **c**, Photoluminescence (PL) spectrum of the cavity-coupled interlayer exciton under excitation with an average power of 100 μW (2.5 MHz repetition rate, central wavelength 640 nm, pulse duration 0.28 ns). The vertical axis corresponds to pixel row indices on the spectrometer camera. **d**, One-dimensional spectrum obtained by integrating the data in **c** from rows 123 to 129. The inset shows the measured spectrum (orange dots) and the fitted curve (grey), which corresponds to a Lorentzian function with a linear background. The fitted FWHM of the Lorentzian function is 0.13 nm.

Sample C serves as a reference device with a modified cavity–emitter coupling configuration. As shown in Fig. S9**a**, the photonic crystal cavity was first patterned into a 300 nm-thick Si_3N_4 layer. Subsequently, a van der Waals stack consisting of hBN (∼30 nm)/WS_2/ WSe_2/hBN (∼10 nm) was transferred on top without additional patterning. The corresponding optical microscope image is presented in Fig. S9**b**. This configuration retains a high cavity quality factor (Q) but exhibits weaker coupling between the interlayer excitons and the cavity mode due to the increased vertical separation between the cavity field maximum and the gain medium.

A representative spectrum from a cavity-coupled interlayer exciton region is shown in Fig. S9**c**. A cavity resonance near 847 nm is clearly observed at the cavity center (around row 125). In contrast to previous samples, where the cavity mode was detected through scattering from regions away from the center, this mode is strongly blue-detuned from the interlayer exciton resonance. Consequently, the exciton background is reduced, allowing direct analysis of the cavity mode at the center. Figure S9**d** displays the integrated spectrum from several adjacent rows in Fig. S9**c**, with the inset showing a magnified view of the cavity resonance fitted by a Lorentzian profile (gray lines). The fitted linewidth of 0.13 nm is resolution-limited, indicating an extremely high Q factor.

This reference sample provides several important insights. First, the cavity design is robust, maintaining a high-Q resonance even when an unpatterned van der Waals stack is placed on top. Second, the interlayer exciton lifetime remains strongly reduced in this non-etched configuration, comparable to that observed in etched samples, confirming that the lifetime shortening in Sample B predominantly arises from Purcell enhancement rather than etching-induced defects. Third, the narrow cavity resonance enables an accurate estimation of the spectrometer resolution.

Power-dependence of the cavity coupled emission

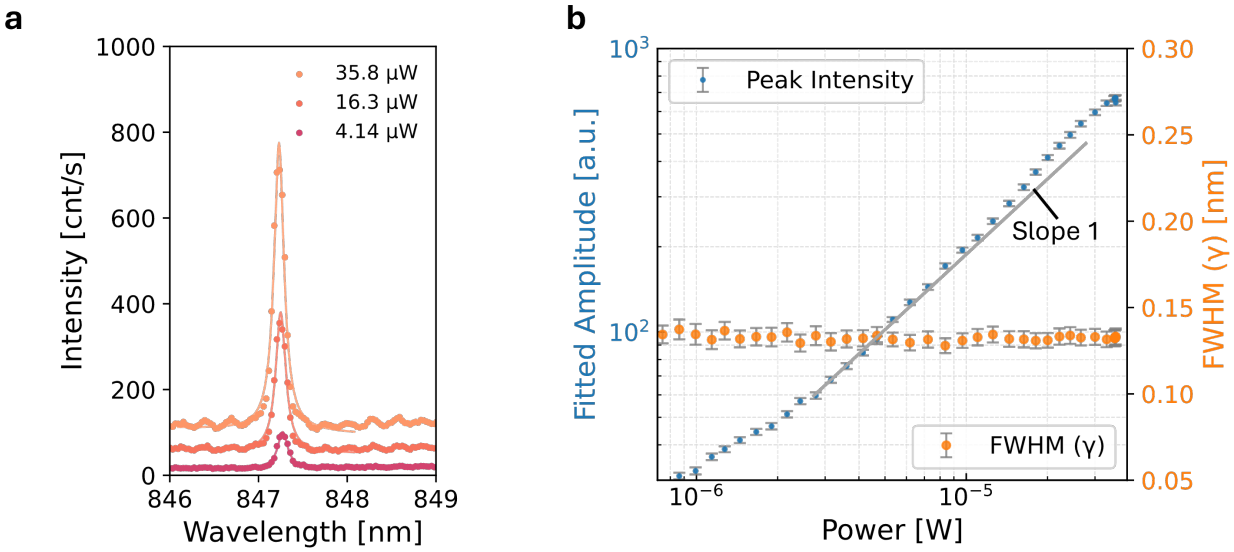

FIG. S10. **a**, PL spectra of Sample C at different excitation powers. The measured data are shown as dots, and the fitted curves (solid lines) correspond to Lorentzian functions with linear backgrounds. **b**, Fitted amplitude and linewidth of the cavity mode as a function of the average excitation power under pulsed excitation (2.5 MHz repetition rate, central wavelength 640 nm, pulse duration 0.28 ns). In both panels, the excitation power refers to the average power of the pulsed laser.

This mode of Sample C does not exhibit a clear nonlinear increase in emission intensity under CW excitation, likely due to suboptimal spatial and spectral overlap between the interlayer exciton and the cavity mode. However, under pulsed excitation, a slight nonlinear increase is observed. The excitation source for these measurements is centered at 640 nm, with a pulse duration of 0.28 ns and a repetition rate of 2.5 MHz.

Figure S10**b** presents the fitted amplitudes and linewidths as a function of the incident power. Between 10 µW and 15 µW, the fitted slope slightly exceeds 1, suggesting the onset of stimulated emission. However, this nonlinear increase is relatively weak, likely counteracted by exciton–exciton annihilation processes (e.g., Auger recombination).

Power-dependent lifetime measurement

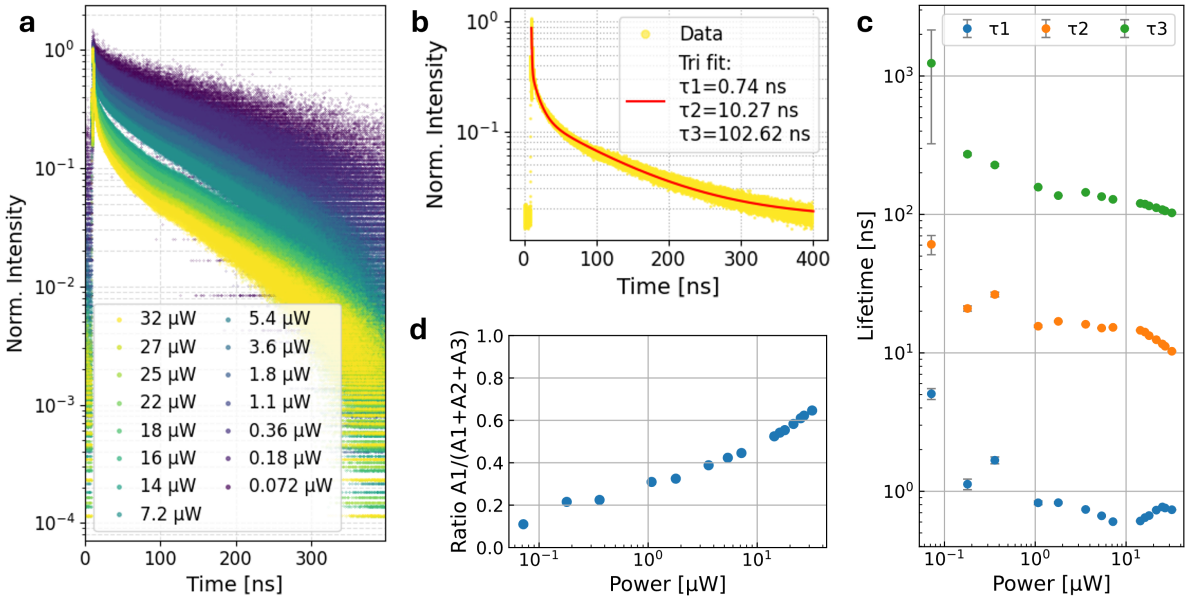

FIG. S11. **a**, Time-resolved PL of Sample C under different excitation powers (2.5 MHz repetition rate, central wavelength 640 nm, pulse duration 0.28 ns). The excitation laser is focused at the cavity center. **b**, Example of tri-exponential fits to extract lifetimes extracted from tri-exponential fits $y(t) = A_1 e^{-(t-t_0)/\tau_1} + A_2 e^{-(t-t_0)/\tau_2} + A_3 e^{-(t-t_0)/\tau_3} + C$. The decay start time was fixed at $t_0 = 10.2$ ns. **c**, Lifetimes extracted from tri-exponential fits $y(t) = A_1 e^{-(t-t_0)/\tau_1} + A_2 e^{-(t-t_0)/\tau_2} + A_3 e^{-(t-t_0)/\tau_3} + C$. The decay start time was fixed at $t_0 = 10.2$ ns. **d**, Relative amplitude of the fastest decay component $A_1/(A_1 + A_2 + A_3)$ as a function of excitation power.

Figure S11 shows the time-resolved PL (TRPL) of Sample C under different excitation powers. The measurements were performed using pulsed excitation at 640 nm with a repetition rate of 2.5 MHz and a pulse duration of 0.28 ns focused at the cavity center. Each decay trace was fitted with a tri-exponential function,

$$y(t) = A_1 e^{-\frac{t-t_0}{\tau_1}} + A_2 e^{-\frac{t-t_0}{\tau_2}} + A_3 e^{-\frac{t-t_0}{\tau_3}} + C,$$

where $\tau_1 < \tau_2 < \tau_3$ denotes three characteristic lifetimes and $t_0 = 10.2$ ns is the fixed start time of the decay. A representative fit is shown in Fig. S11**b**. The extracted lifetimes for different powers are summarized in Fig. S11**c**. Both τ_2 and τ_3 decrease as the excitation power increases, which consistent with the trend observed for Sample B and could be associated with Auger recombination [8]. The fastest component, τ_1, decreases at low excitation levels before saturating at approximately 0.6 ns. We attribute this component to the radiative decay of interlayer excitons coupled to the cavity resonance. Notably, this lifetime closely matches the fastest decay component observed in Sample B after patterning. Since the TMDs in Sample C were not etched, this similarity indicates that the shortened lifetime is primarily a result of Purcell enhancement rather than the introduction of etching induced defects. The relative amplitude of this component, $A_1/(A_1 + A_2 + A_3)$, increases with excitation power as shown in (Fig. S11**c**), suggesting an increased interaction between interlayer excitons and the cavity mode at higher excitation power.

Coherence measurement

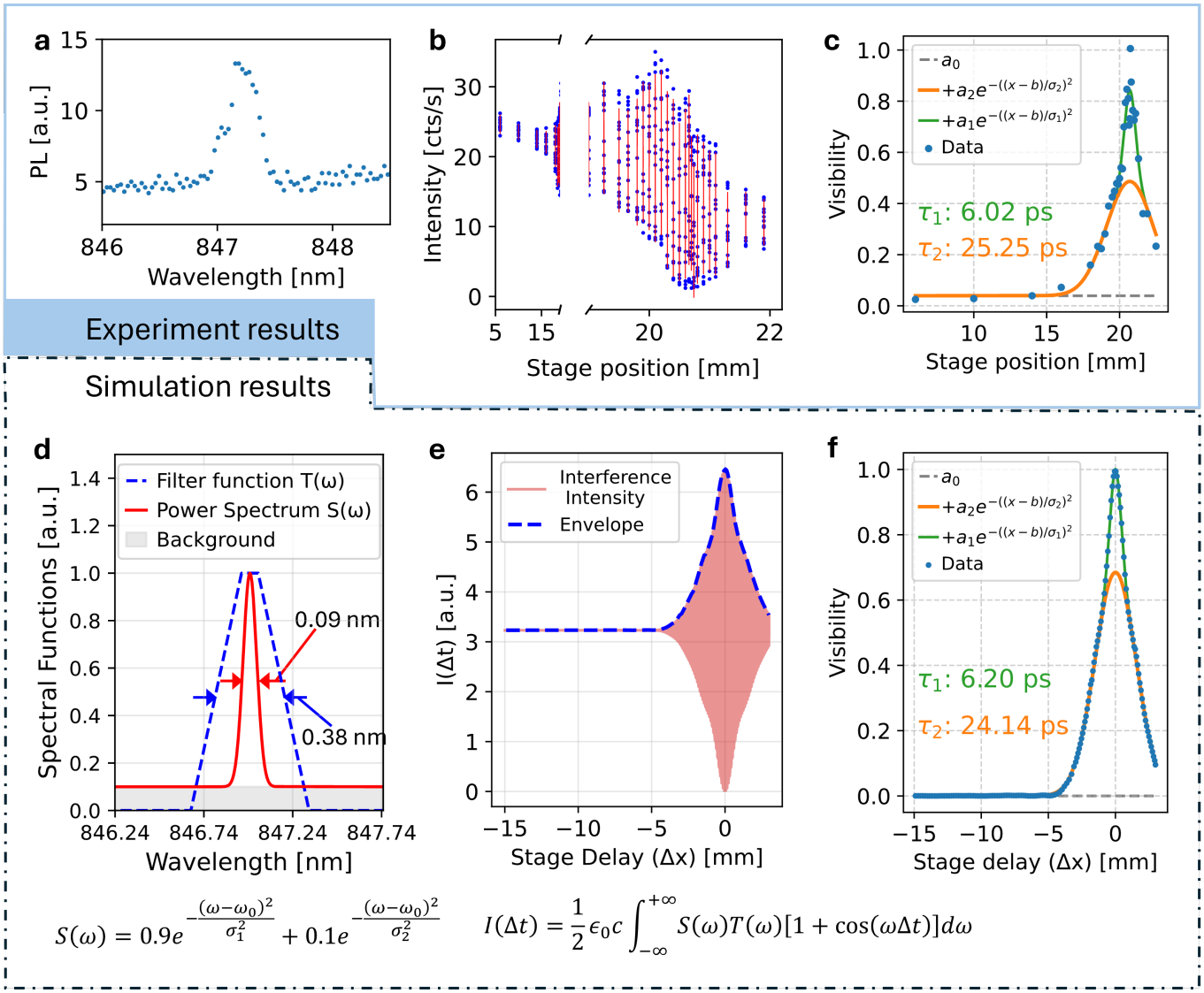

FIG. S12. **a**, PL spectrum of the interlayer exciton coupled to the cavity mode under CW excitation at 54 µW (633 nm). The spectrometer slit width is set to 150 µm. **b**, Interference intensity recorded at the peak pixel of the spectrometer as a function of the delay stage position. A total of 31 delay sets were measured. Each delay set contains 16 data points (blue dots) separated by approximately 90 nm and is fitted with a sinusoidal function (red curve) to extract the visibility. **c**, Extracted visibility from **b** plotted as a function of the delay stage position. **d**, Simulated input spectrum modeled as a Gaussian feature with a FWHM of 0.09 nm and a broad background with a FWHM of 100 nm. The signal and background amplitudes are set to 0.9 and 0.1 respectively. The spectrometer transmission function is modeled as a tapered window with an FWHM of 0.38 nm. **e**, Simulated detector intensity versus delay stage position shown as red solid lines. The interference visibility is then extracted from the envelope indicated by blue dashed lines. **f**, Extracted visibility from **e** as a function of stage delay position. In both **c** and **f**, the blue data points are fitted with a constant background and two Gaussian components using the function $y = a_0 + a_1 e^{-(x-b)^2/\sigma_1^2} + a_2 e^{-(x-b)^2/\sigma_2^2}$. The grey dashed line represents the constant background a_0. The orange curve shows the sum of the second Gaussian and the background. The green curve shows the total fit. The extracted coherence times $\tau_{1,2}$ (calculated from $\sigma_{1,2}$ using Eq. **??**) and are indicated in each panel.

In Sample A, the coherence time of the cavity mode was determined from Michelson interferometry measurements using the spectrometer as the detector. While the spectrometer offers improved signal-to-noise ratio due to its spectral filtering, this approach is not conventional for coherence characterization, raising concerns that the filtering may artificially increase the measured coherence time.

For Sample C, the emission can be collected directly from the cavity center, allowing the cavity mode to be better resolved with a narrower linewidth and higher signal-to-noise ratio. This enables a direct comparison between the linewidth extracted from the Michelson measurement and that obtained from the spectrometer spectrum, thereby validating the spectrometer-based coherence time measurement method. In conclusion, the natural spectral filtering of the spectrometer does not artificially increase the measured coherence time, provided that the cavity resonance is narrower than the spectrometer's filtering function.

The spectrometer slit width was set to 150 µm (same as sample A in coherence measurements) larger than the value used for cavity linewidth measurements in Fig. S10. This wider opening prevents signal clipping, as slight tilting of the moving mirror during delay-stage translation may affect the optical alignment. The increased slit width reduces the spectral resolution. A representative cavity mode measured under this setting is shown in Fig. S12**a**, exhibiting a linewidth significantly broader than 0.13 nm.

Figure S12**b** shows the intensity variation at a single spectrometer pixel corresponding to the cavity resonance as a function of the delay stage position. The extracted fringe visibility is plotted in Fig. S12**c**, which is fitted with the sum of two Gaussian components and a constant background:

$$V(x) = a_0 + a_1 \exp\left[-\left(\frac{x-b}{\sigma_1}\right)^2\right] + a_2 \exp\left[-\left(\frac{x-b}{\sigma_2}\right)^2\right]. \tag{S39}$$

, where $\sigma_{1,2}$ are expressed in micrometers (µm). The corresponding coherence times are calculated using eq. S7.

Among the two fitted components, the one with the shorter coherence time ($\tau_1 \approx 6$ ps) is attributed to the broad signal background. This background is spectrally narrowed by the spectrometer's filtering function, meaning this component reflects the instrumental resolution limit. Based on τ_1 and Eq. S28, we estimate the spectrometer resolution to be 0.38 nm under this setting.

The second component, which exhibits a longer coherence time ($\tau_2 \approx 25$ ps), is assigned to the narrow cavity resonance that exceeds the instrumental resolution. Using Eq. S28, we derive a cavity mode linewidth of approximately 0.09 nm. This value is slightly smaller than the 0.13 nm linewidth measured directly under the highest spectral resolution setting. Since the 0.13 nm linewidth is clearly resolution-limited, the value of 0.09 nm derived from the coherence measurement is fully reasonable.

As a sanity check for our method and analysis, we numerically simulated the expected visibility change by assuming an input signal and the filtering function of the spectrometer pixel. As shown in Fig. S12**d**, the input signal $S(\omega)$ (red curve) consists of a narrow Gaussian feature with a FWHM of 0.09 nm and an amplitude of 0.9, and a broad background with a FWHM of 100 nm and an amplitude of 0.1. The filtering function of the spectrometer pixel $T(\omega)$ (blue curve) was modeled as tapered window with a FWHM of 0.38 nm.

Figure S12**e** shows the simulated intensity on the detector as a function of the delay stage position. Figure S12**f** presents the corresponding visibility as a function of delay, fitted using the same two Gaussian component model. This simulation reproduces the experimental results from Fig. S12**c** well, validating our analysis.

Comment of τ_1 variations

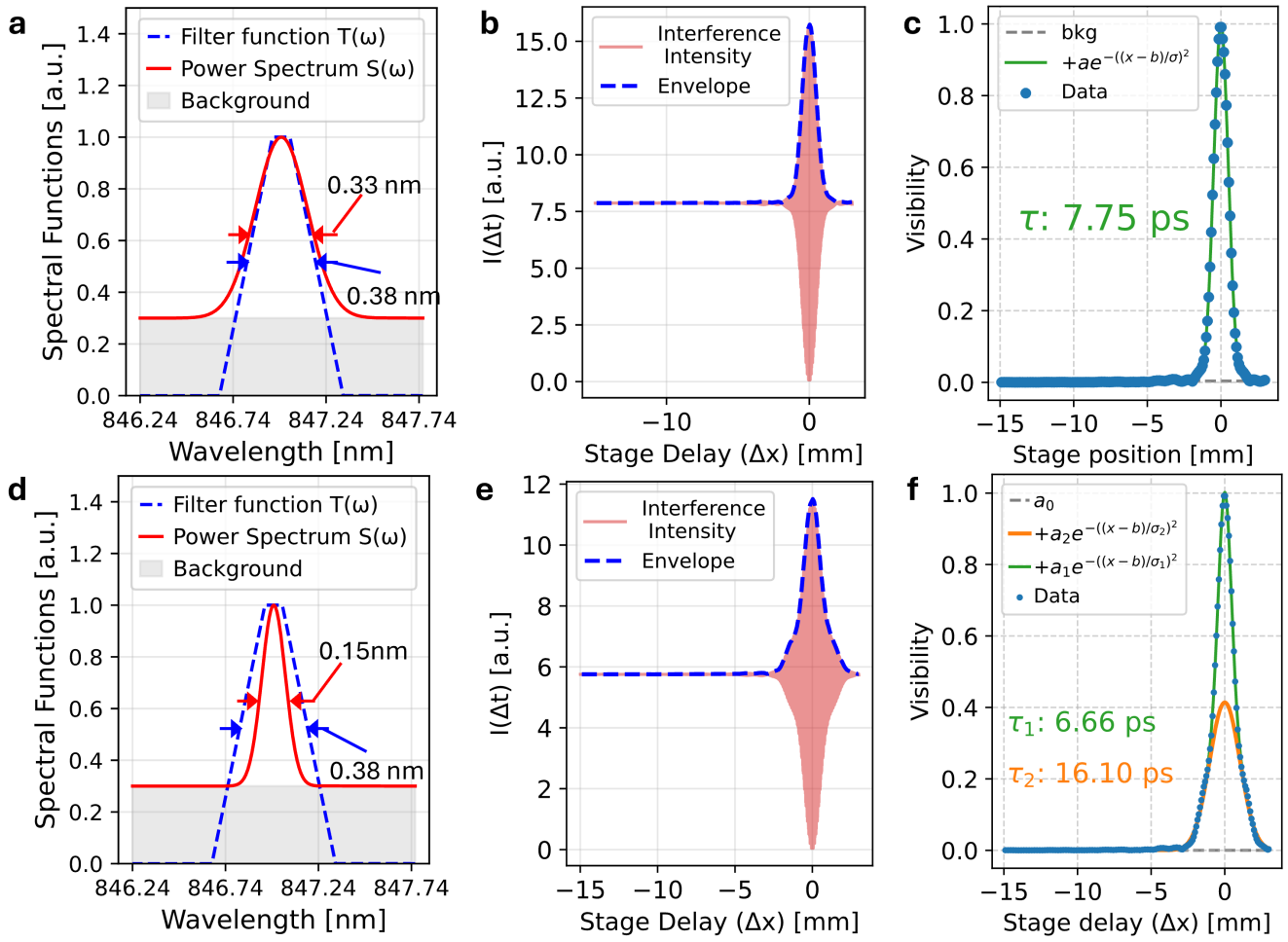

FIG. S13. **a**, Simulated input spectrum modeled as a Gaussian feature with a FWHM of 0.33 nm or **d** 0.15 nm and a broad background with a FWHM of 100 nm. The signal and background amplitudes are set to 0.7 and 0.3 respectively. The spectrometer transmission function is modeled as a tapered window with an FWHM of 0.38 nm. **b**, **b**, Simulated detector intensity versus delay stage position shown (red solid lines) and the envelope (blue dashed lines). **c**, **f** Extracted visibility from **c** as a function of stage delay position. The data in **c** can be fitted with single Gaussian and **f** requires double gaussian for fitting.

We note that while the spectrometer filtering function (FWHM $\approx$ 0.38 nm) remains constant, the extracted τ_1 can vary slightly around 6 ps. This variation is reproduced in our numerical simulations and is primarily attributed to the specific profile of the filtering function and the background emission of the input spectrum.

Two examples are shown in Fig. S13, both assuming the same filtering function profile with a FWHM of 0.38 nm. The narrow Gaussian feature are modeled with a linewidth of 0.33 nm (Fig. S13**a**) and 0.15 nm (Fig. S13**d**) respectively, signal amplitudes are 0.7.

In the first case, where the Gaussian linewidth is close to the resolution limit, the visibility data can only be fitted with one Gaussian component, with a corresponding coherence time of $\tau \approx 7.75$ ps (Fig. S13**c**). This occurs because the filtered background and the cavity mode have nearly identical linewidths, making them difficult to discern.

In the second case, the linewidth of the narrow Gaussian feature is much narrower than the filtering function, allowing two Gaussian components to be distinguished. Here, $\tau_1 \approx 6.66$ ps, which again deviates slightly from 6 ps. This deviation likely stems from the non-Gaussian shape of the filtering function, which prevents the filtered background from appearing truly Gaussian in the visibility data. Fitting this component with a Gaussian is therefore an approximation that can vary depending on the signal-to-background ratio.

Supplementary Note 10. Graphene influence on Cavity

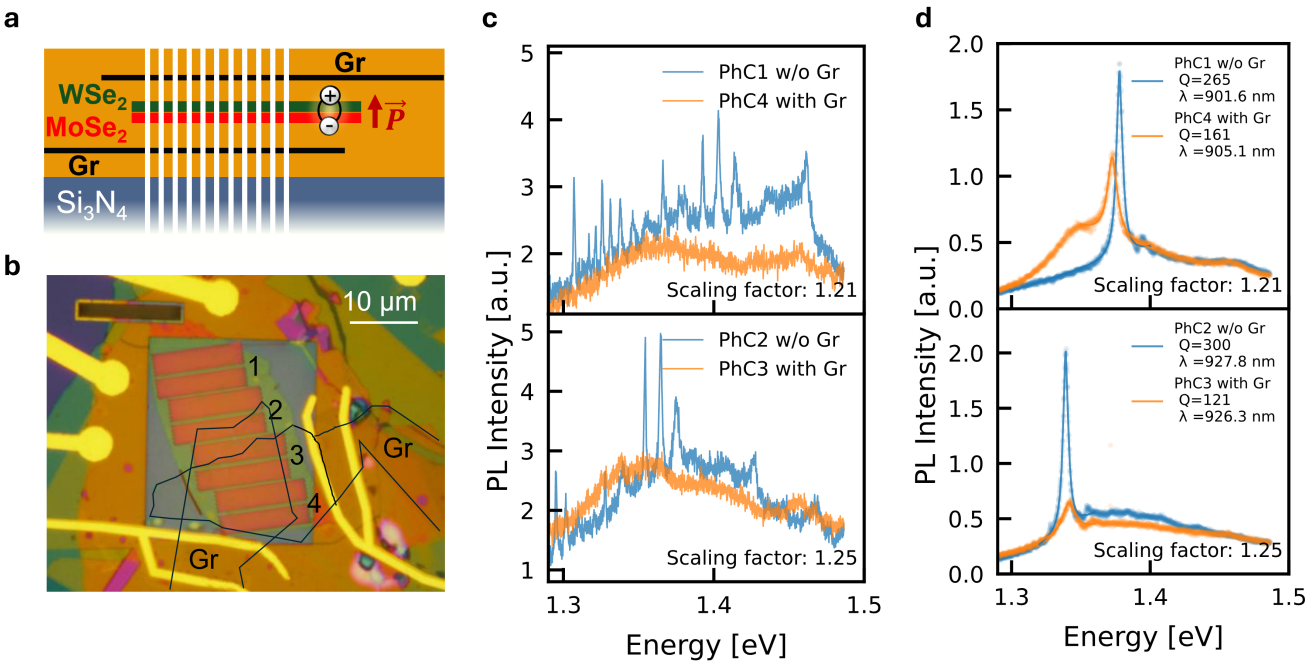

FIG. S14. **a**, Cross-section and **b**, optical microscope image of the device with two graphene field-control electrodes. The stack consists of top/bottom encapsulation hBN (∼30 nm and ∼ 33 nm) and top/bottom gate hBN (∼22 nm and ∼32 nm). The WSe_2 and $MoSe_2$ (CVD-grown) flakes cover four cavities (labeled as PhC1 – 4). Cavities were patterned through the vdW stack and the 200 nm thick Si_3N_4 substrate. Graphene outlines are indicated. **c**, and **d**, Cavity resonances measured from 2D photonic crystal cavities with and without graphene ("with Gr" and "w/o Gr"). All four cavities share the same base design (similar to the cavity used in Sample A) but utilize different in-plane scaling factors. In each panel, the compared cavities have the same in-plane scaling. Spectra in **c** represent light scattered from cavity edges revealing a few high Q modes. **d** shows direct measurements from the cavity center, with the low Q mode fitted with Lorentzian functions on a linear background. All measurements were performed at room temperature.

Cavity resonances are strongly quenched by graphene electrodes due to absorption. As shown in Fig. S14**a** and **b**, we fabricated a device containing two graphene electrodes and WSe_2-$MoSe_2$ TMD heterobilayer. Four cavities (PhC1 - 4) were patterned through the full stack, with PhC3 and PhC4 covered by graphene. To measure the cavity resonance, we pump the cavity center with a focused laser (633 nm, CW, ∼1 mW), and detect the PL from the Si_3N_4 substrate and TMD layers.

Figure. S14**c** shows the spectra obtained from the cavity edges. While cavities without graphene (PhC1 and PhC2) exhibit modes with $Q > 1000$ (blue curve), these resonances are indistinguishable in PhC3 and PhC4 (orange curve). Figure. S14**d** displays the cavity resonance measured from the cavity center, where a prominent, less-confined mode (Q ∼ 200-300) persists despite the graphene coverage. However, the quality factor in these regions is reduced to $Q < 200$. We observed similar quenching in other configurations, such as graphene transferred onto pre-patterned 2D photonic crystals (similar to structure in Fig. S9**a**) or graphene embedded in 1D photonic crystal cavities (cavity geometry based on Ref. [12]). In all such cases, no distinguishable modes with $Q > 1000$ were observed for photonic crystal cavities with graphene. Based on those results, graphene is not suitable for electrodes in high Q cavities.

[1] J. G. E. Gardeniers, H. A. C. Tilmans, and C. C. G. Visser, LPCVD silicon-rich silicon nitride films for applications in micromechanics, studied with statistical experimental design, Journal of Vacuum Science & Technology A **14**, 2879 (1996).

[2] L. A. Coldren, S. W. Corzine, and M. L. Mashanovitch, *Diode Lasers and Photonic Integrated Circuits*, 2nd ed. (Wiley, Hoboken, NJ, 2012) p. 752.

[3] G. Björk, A. Karlsson, and Y. Yamamoto, Definition of a laser threshold, Physical Review A **50**, 1675 (1994).

[4] Y. Li, A. Chernikov, X. Zhang, A. Rigosi, H. M. Hill, A. M. van der Zande, D. A. Chenet, E.-M. Shih, J. Hone, and T. F. Heinz, Measurement of the optical dielectric function of monolayer transition-metal dichalcogenides: MoS_2, $MoSe_2$, WS_2, and WSe_2, Phys. Rev. B **90**, 205422 (2014).
[5] Z. Lian, Y. Meng, L. Ma, I. Maity, L. Yan, Q. Wu, X. Huang, D. Chen, X. Chen, X. Chen, M. Blei, T. Taniguchi, K. Watanabe, S. Tongay, J. Lischner, Y.-T. Cui, and S.-F. Shi, enValley-polarized excitonic Mott insulator in WS2/WSe2 moiré superlattice, Nature Physics **20**, 34 (2024).
[6] S. Chatterjee, M. Dandu, P. Dasika, R. Biswas, S. Das, K. Watanabe, T. Taniguchi, V. Raghunathan, and K. Majumdar, enHarmonic to anharmonic tuning of moiré potential leading to unconventional Stark effect and giant dipolar repulsion in WS2/WSe2 heterobilayer, Nature Communications **14**, 4679 (2023).
[7] A. R.-P. Montblanch, D. M. Kara, I. Paradisanos, C. M. Purser, M. S. G. Feuer, E. M. Alexeev, L. Stefan, Y. Qin, M. Blei, G. Wang, A. R. Cadore, P. Latawiec, M. Lončar, S. Tongay, A. C. Ferrari, and M. Atatüre, enConfinement of long-lived interlayer excitons in WS_2/WSe_2 heterostructures, Communications Physics **4**, 119 (2021).
[8] C.-S. Cai, W.-Y. Lai, P.-H. Liu, T.-C. Chou, R.-Y. Liu, C.-M. Lin, S. Gwo, and W.-T. Hsu, Ultralow Auger-Assisted Interlayer Exciton Annihilation in WS2/WSe2 Moiré Heterobilayers, Nano Letters **24**, 2773 (2024).
[9] D. O. Bracher, X. Zhang, and E. L. Hu, Selective purcell enhancement of two closely linked zero-phonon transitions of a silicon carbide color center, Proceedings of the National Academy of Sciences **114**, 4060 (2017).
[10] J.-M. Gérard, Solid-state cavity-quantum electrodynamics with self-assembled quantum dots, in *Single Quantum Dots: Fundamentals, Applications, and New Concepts* (Springer Berlin Heidelberg, Berlin, Heidelberg, 2003) pp. 269–314.
[11] Lumerical Inc.
[12] C. Qian, V. Villafañe, P. Soubelet, A. Hötger, T. Taniguchi, K. Watanabe, N. P. Wilson, A. V. Stier, A. W. Holleitner, and J. J. Finley, Nonlocal Exciton-Photon Interactions in Hybrid High-Q Beam Nanocavities with Encapsulated MoS_2 Monolayers, Physical Review Letters **128**, 237403 (2022).